

Semi in-situ observation of crack initiation in compacted graphite iron during thermo mechanical fatigue

Lopez-Covalada, Edwin A.; Ghodrat, Sepideh; Kestens, Leo A.I.

DOI

[10.1016/j.ijfatigue.2020.105648](https://doi.org/10.1016/j.ijfatigue.2020.105648)

Publication date

2020

Document Version

Final published version

Published in

International Journal of Fatigue

Citation (APA)

Lopez-Covalada, E. A., Ghodrat, S., & Kestens, L. A. I. (2020). Semi in-situ observation of crack initiation in compacted graphite iron during thermo mechanical fatigue. *International Journal of Fatigue*, 137, Article 105648. <https://doi.org/10.1016/j.ijfatigue.2020.105648>

Important note

To cite this publication, please use the final published version (if applicable). Please check the document version above.

Copyright

Other than for strictly personal use, it is not permitted to download, forward or distribute the text or part of it, without the consent of the author(s) and/or copyright holder(s), unless the work is under an open content license such as Creative Commons.

Takedown policy

Please contact us and provide details if you believe this document breaches copyrights. We will remove access to the work immediately and investigate your claim.



Semi in-situ observation of crack initiation in compacted graphite iron during thermo mechanical fatigue



Edwin A. Lopez-Covaleda^{a,b,*}, Sepideh Ghodrati^c, Leo A.I. Kestens^{a,d}

^a Metals Science and Technology Group, EEMMeCS Dept., Ghent University, Technologiepark 46, Ghent 9052, Belgium

^b Metal Processing Group, CRM GROUP, Technologiepark 48 B, 9052 Gent, Belgium

^c Department of Design Engineering, Faculty of Industrial Design Engineering, Delft University of Technology, Delft, the Netherlands

^d Materials Science and Engineering Department, Delft University of Technology, Mekelweg 2, Delft 2628 CD, the Netherlands

ARTICLE INFO

Keywords:

Thermo-mechanical fatigue
Compacted Graphite Iron
Paris crack-growth law
Semi in-situ
Crack initiation

ABSTRACT

Compacted Graphite Iron is a suitable material for the engine cylinder heads of heavy duty trucks. In the base of the cylinder head, the Valve Bridge is subjected to Thermo-Mechanical Fatigue as a result of daily start-up and shut-down operational cycles. With the aim to investigate crack initiation, a semi in-situ experiment was conducted by employing a disassemblable dog-bone sample. The procedure consisted of iteratively interrupting a thermo-mechanical fatigue test to observe the evolution of the microstructure by Scanning Electron Microscopy, and Electron Backscatter Diffraction. Finishing the first thermo-mechanical fatigue cycle, edge delaminated graphite particles were observed to be connected by cracks. Cyclic plastic strain computation showed that edge graphite particles can interact by overlapping plastic zones that arise at the tip of the delamination cracks and thus provide a crack propagation path. Finally, the electron backscattered diffraction technique allowed to observe the competition between recovery and plastic strain during the first few thermo-mechanical fatigue cycles.

1. Introduction

Conventional mechanical testing rigs are dedicated devices to accurately measure material response to imposed boundary conditions such as strain, stress or temperature. However, this approach does not allow to precisely monitor the microstructural evolution occurring during the test and inevitably, microstructural characterization has to be performed before and after the test. Alternatively, in-situ observation tests aim to monitor the microstructural changes while the material is under mechanical or thermal load. In-situ techniques require to be carefully tuned for specific applications; e.g. heat treatments [1,2] or mechanical tests can be performed in TEM [3,4], SEM [5–7], X-Ray diffraction [8,9] or Micro-Tomography [10] facilities. This allows to observe in-situ phenomena such as slip, texture change, dynamic recrystallization or damage under external loading conditions. Although, this is a suitable technique to gauge the effect of external boundary conditions to local microstructural changes, the procedure has some limitations as it cannot always be guaranteed that the in-situ loading conditions are truly representative for the acting loading conditions

during operational use of a material nor can it be guaranteed that the in-situ test can be compared flawlessly with standard testing methods. Differences between in-situ and standard testing conditions may occur in terms of sample size, gripping conditions, loading rate and capacity, atmospheric conditions and heating or cooling rates among others.

Severe loading conditions may arise in some engine components such as exhaust manifolds [11–13] and cylinder heads [11–13] in heavy duty truck engines. In particular, the valve bridge (VB) areas located between the intake and exhaust valve bores of the diesel engine cylinder head are under continuous Thermo-Mechanical Fatigue (TMF) conditions. Restrictions, related to mechanical fits, fixations, misalignments and temperature distribution along the cylinder head, lead to constrained thermal expansion during engine start-up (leading to high temperature compression at the VB), and retention of thermal contraction after engine shut down (leading to room temperature tension in the VB). Such loading condition is also known as Out of Phase (OP) Thermo-Mechanical Fatigue because the lowest (compressive) stress is obtained at highest temperature and vice-versa. Some authors have also considered the effect of super imposed high cycle fatigue associated

Abbreviations: *a*, defect size; AC, as cast; CGI, compacted graphite iron; IP, in phase; LD, loading direction; OP, out of phase; SEM, scanning electron microscopy; TMF, thermo-mechanical fatigue; C_p , paris' crack growth law factor; *E*, elastic modulus; VB, Valve bridge

* Corresponding author.

E-mail addresses: edwinalexis.lopezcovalada@ugent.be (E.A. Lopez-Covaleda), S.Ghodrati@tudelft.nl (S. Ghodrati), Leo.Kestens@UGent.be (L.A.I. Kestens).

<https://doi.org/10.1016/j.ijfatigue.2020.105648>

Received 11 November 2019; Received in revised form 10 March 2020; Accepted 9 April 2020

Available online 22 April 2020

0142-1123/ © 2020 Elsevier Ltd. All rights reserved.

with engine combustion cycles [14,15]. This research has consistently found the existence of a threshold high cycle fatigue strain range that rapidly reduces the TMF lifetime. The threshold is a function of material and temperature range. This phenomenon has been modeled based on replica observations that revealed the micro mechanisms that accelerate crack propagation as soon as a critical crack length is reached [16].

In literature reports on OP TMF in Compacted Graphite Iron (CGI), the crack initiation and lifetime have been studied under experimental conditions that aim to reproduce the real engine operational conditions until failure [17,18], whereby microstructural results are reported on post-mortem samples or samples obtained from interrupted tests [19]. Crack initiation and propagation can be monitored in real time in a SEM microscope equipped with an in-situ test rig suited for OP TMF. For instance, Zhang and Liu [20] used notched aluminum specimens to speed up the crack initiation and monitor the crack propagation. They observed crack closure during compression, and uniform crack growth only in a fraction of the tensile part of the cycle. Despite their important findings, the test was limited to plane stress condition (sample thickness and width 0.86 and 8 mm, respectively). Likewise, Jacobsson et al. [21] carried out in-situ isothermal fatigue tests on Inconel 718 samples. Both In Phase (IP) and OP TMF modes were applied with two different temperature ranges, from 300 °C to 550 °C, and from 300 °C to 630 °C, respectively. The comparison showed that maximum temperature of IP and OP TMF was a decisive parameter for crack propagation rate and fracture morphology. However, the size of the testing device involved limitations in heating and cooling rates since the former was achieved by electrical heating of the gauge length, whereas the latter was obtained by cooling the sample grips. Concerning cast iron, Norman et al. [22] performed in-situ fatigue tests on compacted, nodular and flake cast irons. In their research a constitutive model was developed that was validated at the delaminated interface between metal matrix and graphite. Stress concentration locations, measured by micro digital image correlation, were identified in the surroundings of the interface.

In order to combine the boundary conditions of a conventional TMF testing equipment with monitoring the microstructural evolution during the test, in this research a semi in-situ approach was developed. Respecting the sample dimensions described in the European Code of Practice [23], a testing setup was designed that allowed to disassemble the TMF sample for intermediate microstructural observation. The semi in-situ approach is an approximation of a fully in-situ test, whereby a single sample is monitored for mechanical and microstructural characterization in subsequent steps.

Although the effects of thermal and mechanical loads on CGI tested under TMF were well investigated by monitoring the stresses evolution [24], the role of graphite in crack initiation is not well-documented considering the current literature. Therefore, the aim of this study is twofold: (i) to monitor the CGI microstructural evolution under TMF loading conditions and (ii) to link the microstructural observations to macroscopic mechanical properties.

2. Materials and methods

2.1. Materials and microstructural characterization

CGI was obtained from cast ingots of which the microstructure was quantitatively characterized based on 20 optical microscopy images ($1 \times 1 \text{ mm}^2$). The microstructure consisted of 10.0% compacted graphite with vermicular morphology, 2.5% spheroidal graphite, 3.7% ferrite, and pearlite by balance. The pearlite average interlamellar space was $0.67 \mu\text{m}$ ($\pm 0.23 \mu\text{m}$) (cf. Fig. 1), while the average pearlite grain size was found to be $(112 \pm 46) \mu\text{m}$ giving rise to the Vickers hardness value of $256 (\pm 12) \text{HV1}$. Further mechanical properties and chemical composition can be found elsewhere [24]. The geometrical and dimensional features of the graphite phase were quantified by post-processing secondary electron (SE) Scanning Electron Microscopy (SEM)

images using ImageJ software [25] (e.g. Fig. 2) (SEM of type FEI Quanta 450® with field emission gun filament). From the quantitative output, listed in Table 1, it can be seen that the graphite length and density exhibit a large variation, reflecting the heterogeneous graphite distribution already shown in Fig. 2.

2.2. TMF setup

The semi in-situ test was carried out on a servo-hydraulic MTS® uniaxial testing machine (cf. Fig. 3) controlled by the MultiPurpose TestWare® software. The TMF test was performed under strain control mode whereby the axial strain is measured by a strain gauge extensometer, attached with two contact ceramic rods to the specimen gauge length (12 mm). Heating and cooling cycles between 50 and 420 °C were achieved by using a high frequency induction generator (297 kHz and 5.9 kW) attached to a barrel type coil for heating while cooling was imposed by blowing compressed air through nozzles around the gauge length. The heating and cooling rates were 7.4 and 5.3 °C/s, respectively, in accordance with the European code-of-practice [23]. The holding time of TMF tests at both high and low temperatures was set to 30 s. Temperature was measured and controlled by a flattened ribbon contact type K thermocouple attached to the middle of the sample gauge length (springs were implemented to firmly maintain the contact thermocouple-sample). In order to verify axial temperature uniformity, two additional thermocouples were placed at 1 mm below and above the central thermocouple that was used for control purposes, in agreement with the European code-of-practice [23].

Further setup details are well described elsewhere [17,24,26].

2.3. Testing methodology

In order to monitor the microstructural evolution and crack initiation, the TMF test was chosen to be carried out in a semi-in-situ mode, whereby the test was interrupted at specific stages or steps (cf. Fig. 4). The test was performed in the so called total constraint mode [17,26], whereby the sample gauge length is constant during the entire test. Thereby all the thermal expansion and contraction due to heating and cooling are completely converted into mechanical strain (compression and tension, respectively). This test was performed on a specially designed specimen so as to allow monitoring one particular microstructural site. Various conditions were considered as follows: condition (0) (cf. Fig. 4) corresponds to the initial machined condition, condition (1) corresponds to the end of the first heating stage, condition (2) corresponds to the end of the high temperature holding time of the first cycle, condition (3) corresponds to the end of the low temperature holding time of the first cycle, condition (4) corresponds to the end of the heating of the second cycle, and condition (5) corresponds to the end of the high temperature holding time of the second cycle. Additionally conditions (6) and (7) were monitored, at the end of the 5 and 10th cycle, respectively.

2.3.1. Semi in-situ sample considerations

In the semi in-situ experiment under consideration, a full constraint TMF test was interrupted for microstructural characterization by SEM-EBSD. To the purpose of observing one specific microstructural site, it was necessary to redesign a standard TMF dogbone sample.

Although the reference specimen shape was preserved [17,24] the solid specimen was substituted by a specimen that could be split in two halves along the loading axis, cf. Fig. 5. The specimen was manufactured from ingot material starting from a cuboid shape of $5 * 5 * 15 \text{ cm}^3$. By appropriate machining operations the disassemblable specimen was obtained. The free flat surfaces appearing on the split sample were manually prepared for metallographic observation, i.e. polished with diamond paste and finished with colloidal silica ($0.05 \mu\text{m}$) polishing for 30 min.

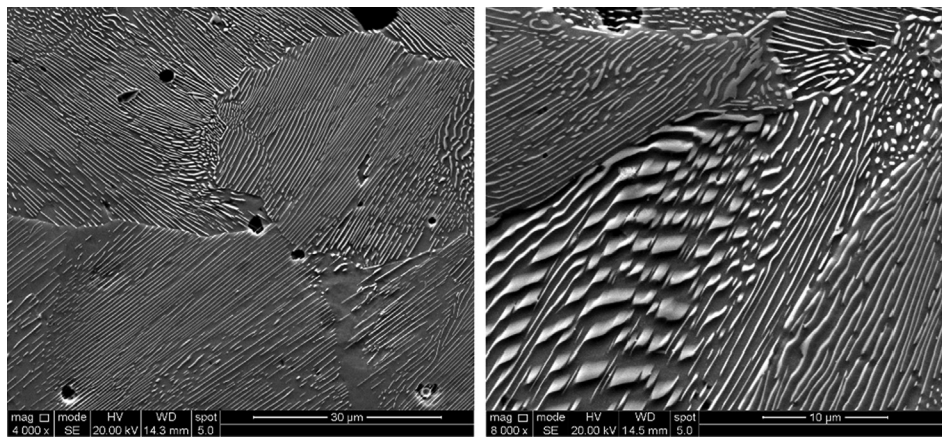


Fig. 1. Etched As Cast ingot material in order to determine grain size and pearlite interlamellar spacing. Plates of cementite (white) and ferrite (black) can be discerned, forming lamellar pearlite.

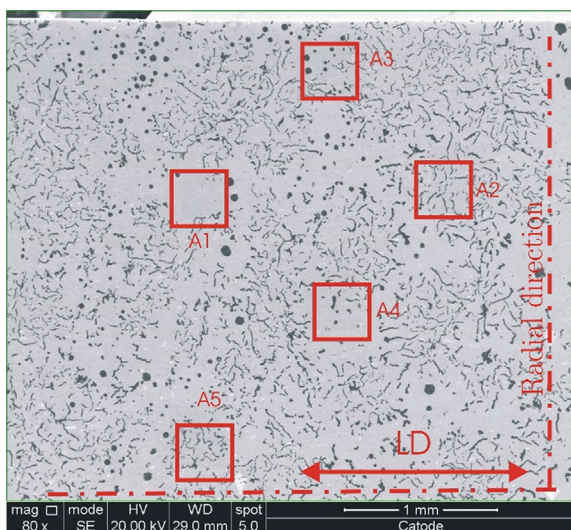


Fig. 2. SE image taken at the center of the internal flat face of the semi in-situ half sample; i.e. the section spanned by the Loading Direction (LD) and the radial direction (perpendicular to LD). Areas A1 to A5 are regions of interests scattered over the full section.

Table 1

Dimensional characteristics of graphite measured in ingot material; average value and distribution standard deviation.

Graphite characteristic		Value (\pm)
Density	[particles/mm ²]	290.12 (63.8)
Compact/Flake	Thickness [μ m]	4.95 (3.2)
	Length [μ m]	44.67 (39)
Nodules	Nodularity [%]	19.29 (7.8)
	Diameter [μ m]	19.0 (10)

2.3.2. Semi in-situ TMF test considerations

The semi in-situ TMF sample was positioned in the TMF machine before each TMF step of Fig. 4 by applying the following three steps approach: First, before sample assembly, and using ink, the sample center (axial direction) was marked on the external sample surface. Second, the previous mark in the assembled sample was placed so as to coincide with the axial center of the machine induction coil (cf. Fig. 3). Third, the K thermocouple of the TMF system was placed at the sample ink mark.

The seven TMF steps of Fig. 4 were intended to capture the microstructural evolution during the first cycles of full constraint OP TMF.

In order to minimize the influence of interrupting the test and removing the sample from the machine, arrest and resume operations were carefully planned, executed and monitored. On the one hand, to arrest the test, the force was dropped in 0.5 s while temperature was reduced as fast as possible to room temperature by blowing compressed air and cutting the current in the heating induction coil. On the other hand, to resume the test, force and temperature were simultaneously raised in 15 s to the last recorded values before arresting the test in the previous step.

2.3.3. Semi in-situ SEM considerations

The split shape of the sample was necessary in order to observe the bulk microstructural evolution on the internal face of the semi in-situ halves, whereby the specimen size was limited by the size of the SEM chamber. The internal sides of both halves of the sample were carefully observed to the purpose of observing morphology variations, i.e. delamination or cracks. Furthermore, in order to carry out EBSD measurements, a dedicated sample holder was designed (cf. Fig. 6 “Pretilted sample holder”). In spite of the fact that both internal flat planes of the semi in-situ sample were metallographically prepared before and after sample manufacturing, each TMF step produced a thin blue layer of oxide that was carefully removed by manual polishing using colloidal silica (0.05 μ m) for five minutes or less. To localize the sample center, Vickers indents were used. It was revealed that polishing the oxide layer removed on average 1.3 μ m of the material surface.

The microstructural evolution was recorded by EBSD scanning using a step size of 0.5 μ m on the five different sites (A1 up to A5) with a size of 400 * 400 μ m² each, cf. Fig. 2. The average misorientation between each pixel and its first neighbors (also known as Kernel average misorientation or KAM) was calculated. Similarly, the entire area (3,000 * 3,000 μ m²) in Fig. 2 was scanned. Given its size it was necessary to increase the step size to 4 μ m.

3. Results

Dedicated images from SEM were recorded along the internal side of both halves of the smooth semi in-situ sample, before and after each TMF step (cf. Fig. 4).

The observations started at the step zero (as machined condition) tracking one hundred particles distributed from the edge to the core of the samples in the center of the gauge length. At this point neither graphite particles nor the sample surface contained observable damage (delamination nor cracks). During the first half of the first TMF cycle, corresponding to steps 1 and 2, (high temperature compression) no damage was observed.

It was only after the introduction of a tensile stress during the

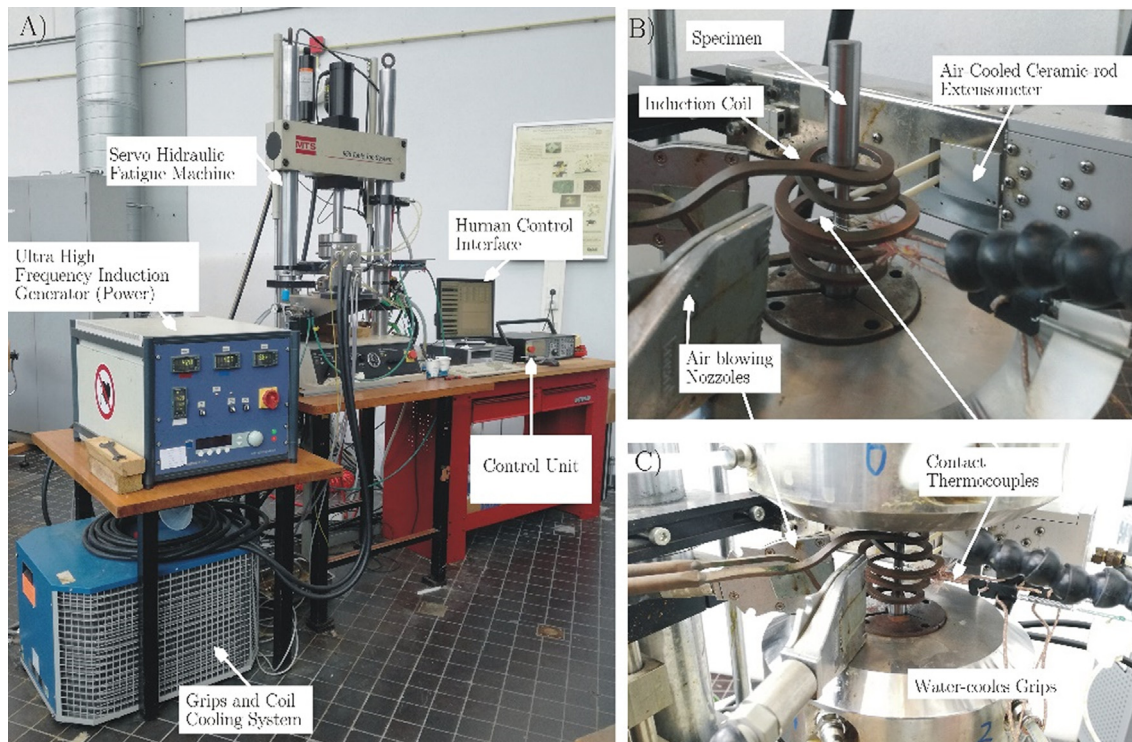


Fig. 3. Servo hydraulic MTS machine used for TMF tests.

cooling stage at the end of the first cycle (step 3 in Fig. 4) that two important phenomena emerged: delamination of the metal matrix from graphite particles and connection of graphite particles by short cracks. Such phenomena were clearly observed in two areas of the sample: in the bulk and at the edges (cf. Fig. 7A). In the bulk area only particles approximately perpendicular to the Loading Direction (LD) were delaminated (cf. Fig. 7B). In contrast, along the sample edges, most of the graphite particles were delaminated and some neighboring compacted graphite particles were connected by an extended crack that appears to have been arrested after linking one or two graphite particles (cf. Fig. 7C). Although the observation of the sample edge was limited to an arbitrary 2D plane, it could be seen that the cracks propagated more frequently across vermicular graphite clusters than across isolated particles. Conversely, nodular graphite particles were not linked by cracks, even being initially delaminated from the matrix and located at the sample surface. The 2D measurement of cracks at the end of the first cycle (step 3) revealed that the initial crack size varies between 80 μm and 120 μm (measured perpendicular to the loading direction).

The identified edge cracks and bulk delaminated particles were traced down to step 7 (cf. Fig. 4), which correspond to 10 TMF cycles.

However, no further growth was observed neither of the edge cracks nor of bulk delamination. The Paris' crack growth law was used to estimate the crack growth rate. It was found that 13 cycles would be required to produce 10 μm of growth from a stable crack of 80 μm at the sample surface. Since only 10 cycles were applied and no crack growth was revealed, it is inferred that crack propagation was not possible to be measured due to the necessary polishing steps that removed in total $\sim 9.1 \mu\text{m}$ depth. In consequence material removal could have hidden the observation of crack propagation.

By observing the maximum stress values in Fig. 8, the strain hardening behaviour is revealed (circle data points). The individual values as well as the trend are in accordance with previously reported test data gathered on identical material in conventional uninterrupted TMF full constraint tests [24]. The figure reveals the matrix average KAM evolution during the semi in-situ test. Regarding the evolution from step zero to one, the figure indicates that the large KAM value measured before testing is rapidly reduced. The latter shows that high temperature lead to recovery of the lattice defects (sensitive to the KAM parameter) introduced by sample manufacturing and TMF compression during the first TMF step. Consequently, between steps one and two, the

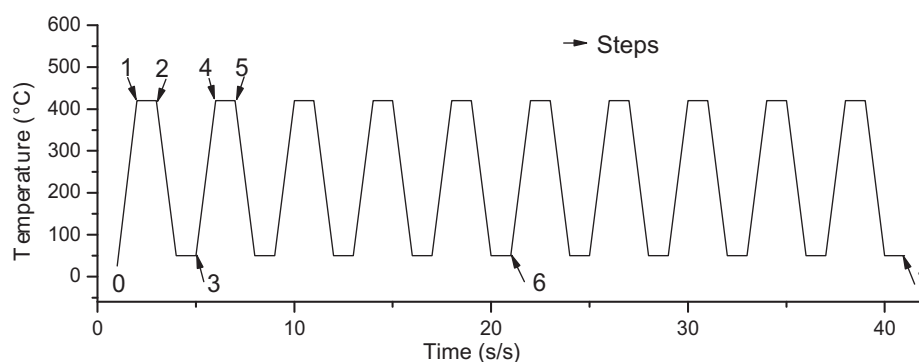


Fig. 4. Schematic of applied temperature during semi in-situ TMF test. A total of 10 cycles were applied whereby the test was interrupted for microstructural observation at every step from 1 to 7. The reference condition 0, is the condition of the sample surface after machining and metallographic sample preparation.

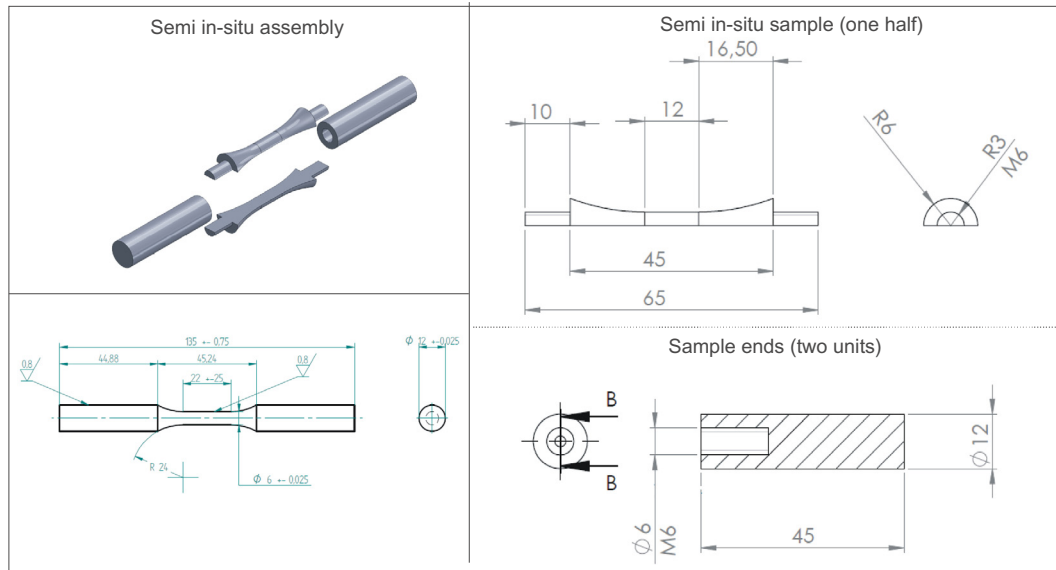


Fig. 5. Semi in-situ sample assembly and detailed view of the components.

reduction in average KAM persisted during the holding time under the action of high temperature and mechanical compression load. Next, from the second to the third step, the first TMF cycle finishes by switching from compression to tension, and from high to room temperature. The new condition has led to a subtle increase of the KAM reflecting the introduction of lattice defects due to plastic strain in tension and absence of temperature activated recovery.

The second cycle was initiated at step 3 and arrested after the heating stage at step 4. Although this cycle fraction is equivalent to the interval from zero to one, the KAM reduction was not as significant as in the first cycle. The latter indicates that the lattice defects introduced in the microstructure due to sample manufacturing was significant and the action of keeping the sample at 420 °C during 30 s in the first cycle strongly enhanced recovery. Nevertheless, during the temperature rise stage of the second cycle (from step 3 to 4) only a minute KAM reduction was observed since significant recovery has already occurred in the previous cycle. From the second cycle onwards, the average KAM value rises slightly with the number of steps and cycles indicating that damage is being accumulated due to compression and tension and that the effect of temperature is less effective. This behavior, is a clear a reflection of the competition between recovery and damage due to cyclic plastic strain.

4. Discussion

It is evident that the proposed semi in-situ technique might raise questions on the microstructural statistical relevance and issues regarding reliability or reproducibility. E.g. there may be side effects of interrupting the test (involving replacing the sample, fast heating and cooling rates, among others factors) on the mechanical response. Concerning the microstructure evolution, the cross section in the semi in-situ sample is generally larger compared with the one observed in an in-situ sample [6,8]. By performing larger field observations (e.g. SEM and EBSD) the statistical relevance is improved. However, replacing the sample and re-alignment might have affected the mechanical response and such effect is accumulated as more steps are performed. In order to mitigate such effects, the current procedure was limited to the first 10 cycles and was interrupted only seven times, focusing on the first cycle (two steps) and afterwards extending the gap between observations.

Concerning the adverse effect of concentrated thermal stresses due to high cooling rates (in the arresting procedure), it can be said that cooling is an operation related to the transition from compression stress to zero stress. The compression linked to thermal gradients would not be related to delamination but to residual compression stress, of which the positive effect might interact with the negative effect of sample misalignment during repositioning. Unfortunately such effects are

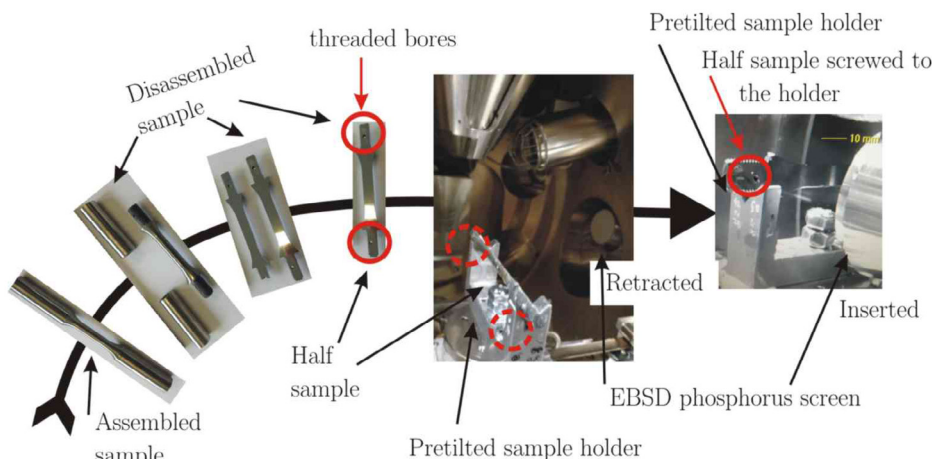


Fig. 6. Disassembling procedure of semi in-situ dog bone sample for EBSD observation.

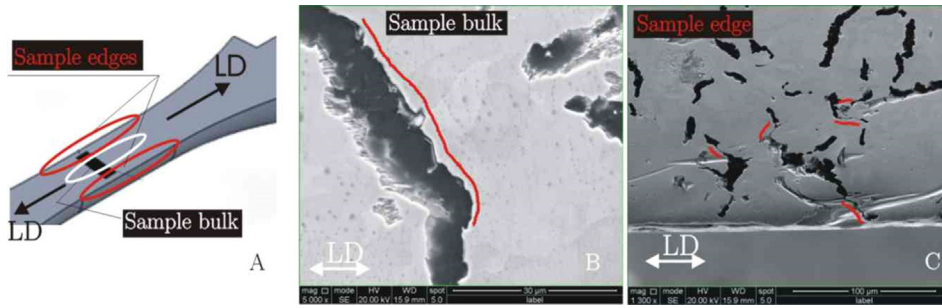


Fig. 7. SEM images of the semi in-situ sample edges and bulk at the end of the 1st cycle (step 3).

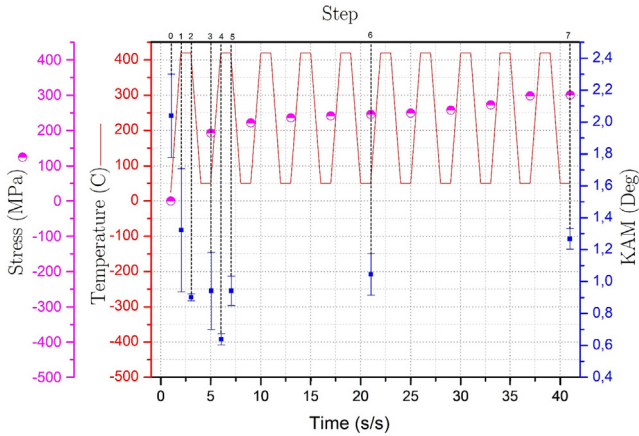


Fig. 8. Schematic temperature, measured maximum tensile stress, and KAM evolution of the matrix of the semi in-situ sample. Error bars on the average KAM values represent the standard deviation of KAM distribution function.

difficult to discern and quantify.

Regarding the reproducibility of the technique, two considerations can be made: I) it can be validated by comparing stress values observed in the semi in-situ experiment with results obtained from conventional uninterrupted tests on solid (not disassemblable) samples, tested under the same boundary conditions. The conventionally tested samples were machined from the same original material [24]. In the first cycle of such conventional uninterrupted tests, a maximum stress was found of 218.4 (± 10.4) MPa, whereas for the semi in-situ test a value was observed of 198.12 MPa. The difference might have originated from the effect of arresting the test twice before reaching the end of the first cycle; II) furthermore, solid and disassemblable samples developed a hardening rate of 10% and 15% in the first cycle, respectively, which is an indicator of satisfactory reproducibility of the semi in-situ test.

The detailed and sequential SE image observation showed that the crack was initiated at the end of the first TMF cycle, corresponding to room temperature and tensile stress, along the sample edges, whereas only delamination was observed in the bulk of the sample (in the same step). Furthermore, it was found that cracks were the result of joining graphite particles that were grouped in clustered areas, which is in accordance with the graphite density observations, cf. in Table 1. It is relevant to emphasize that cracks were initiated at sample edges of the smooth specimen. According to fracture mechanics [27,28] an approximate elliptical bulk crack of length 2a corresponds to a semi-elliptical edge crack of length a. In consequence, and according to Irwin [28] for a given crack length a, the plastic zone in front of a defect or crack (Eq. (1)) is doubled when the defect is open to the surface. Irwin's calculation involved the stress intensity factor in load mode one K_I [27,28] (see Eq. (2)), whereby the defect size is taken as a (not 2a), and $f(g)$ represents the shape factor according to Tada [29] (see Eq. (3)).

$$r_y = \frac{1}{\pi} \left(\frac{K_I}{\sigma_y} \right)^2 \quad (1)$$

$$K = \sigma \sqrt{2\pi a} f_g \quad (2)$$

$$f_g = \frac{1}{\left(1 - \frac{a}{r}\right)^{3/2}} \left(1.122 - 1.302 \left(\frac{a}{r}\right) + 0.988 \left(\frac{a}{r}\right)^2 - 0.308 \left(\frac{a}{r}\right)^3 \right) \quad (3)$$

Since delamination was observed in the sample bulk, under total constraint, during the first TMF cycle, it is evident that the bonding between graphite and matrix [30] was broken. Therefore, it is reasonable to compute Irwin's plastic zone in front of a crack as a function of the crack length which, corresponds to the delaminated size of the graphite particle (length). Employing Eqs. (1)–(3), Fig. 9 was constructed using the maximum experimentally measured stress of 288 MPa (i.e. maximum stress of the full test) in total constraint experiments using solid samples tested until failure [24]. Fig. 10 shows a schematic of the cyclic plastic zone at the tip of the crack perpendicular to the main loading direction (vertical direction in Fig. 10). According to literature [31,32], the cyclic plastic zone is equal to 1/4 of the monotonic plastic zone (Eq. (1)). Fig. 9 and Fig. 10 can be used to explain the effect of the plastic zone at the end of the first TMF cycle as a consequence of the presence of delaminated graphite particles. For instance, if 44.67 μm is taken as the average graphite length (see Table 1), and assuming that graphite particles were completely delaminated, it can be seen in Fig. 9 that the dynamic plastic zone rises from 5 to 10 μm comparing bulk to edge particles.

Regarding the latter example, it is reasonable to propose that the semi in-situ measured crack size (from 80 μm to 120 μm) is the result of adding the average graphite length (44.67 μm) to the average distance between graphite centroids (59.5 μm) which is bridged by the

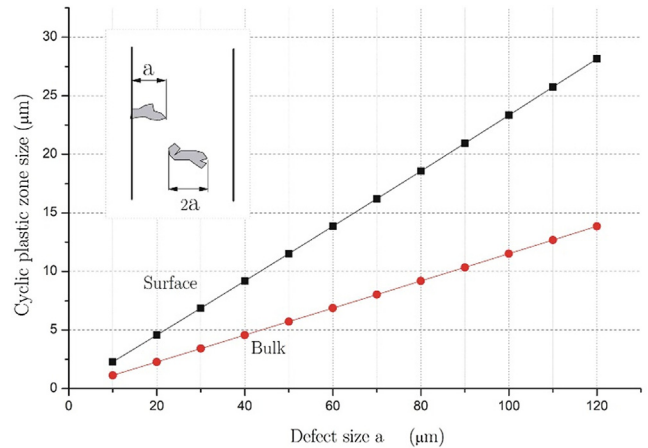


Fig. 9. Plastic zone in front of a defect under cyclic loading derived from Irwin's equation corrected for cyclic plasticity. Calculation obtained by using data from solid smooth specimens tested under full constraint until mode failure [24].

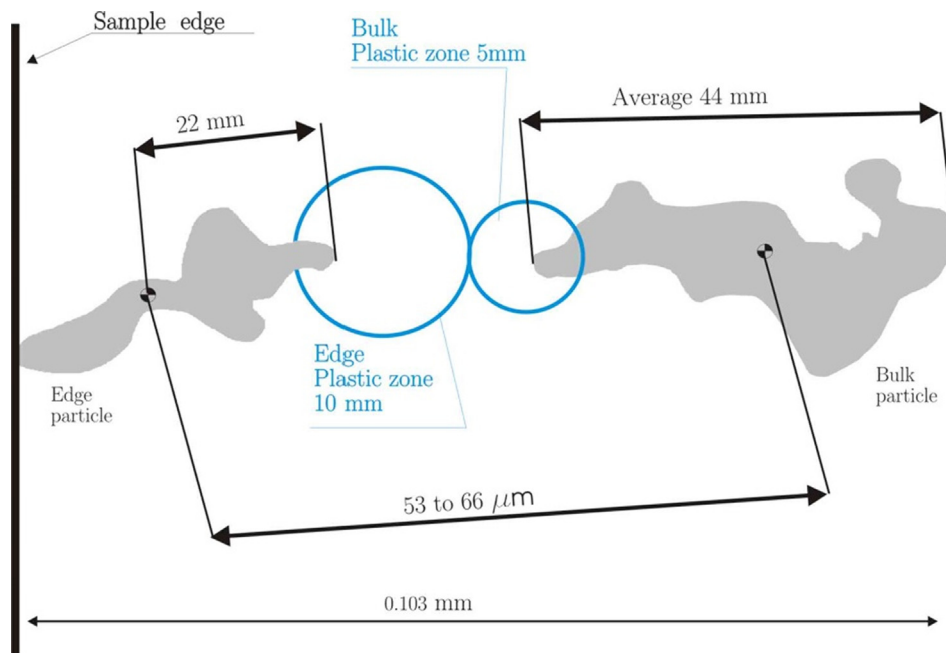


Fig. 10. Crack initiation model considering delamination and the cyclic Irwin plastic zone.

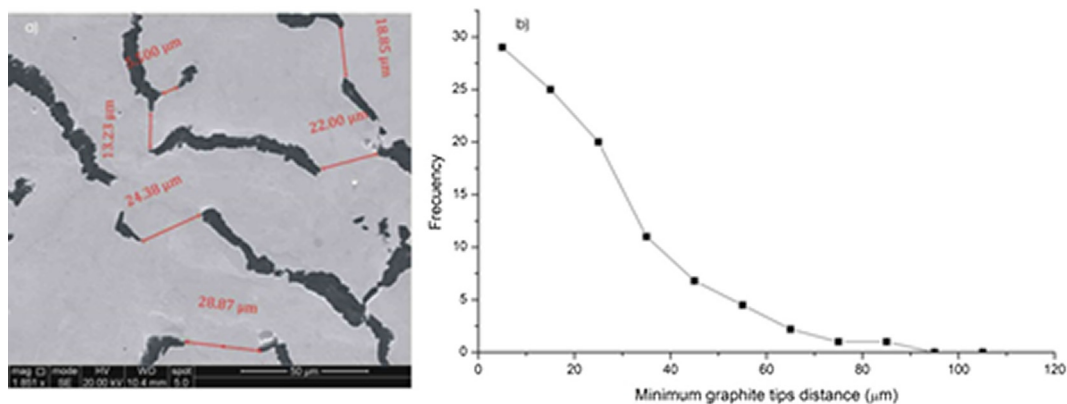


Fig. 11. (a) Minimum distance between delamination crack tips associated with graphite particle and (b) distribution of this variable.

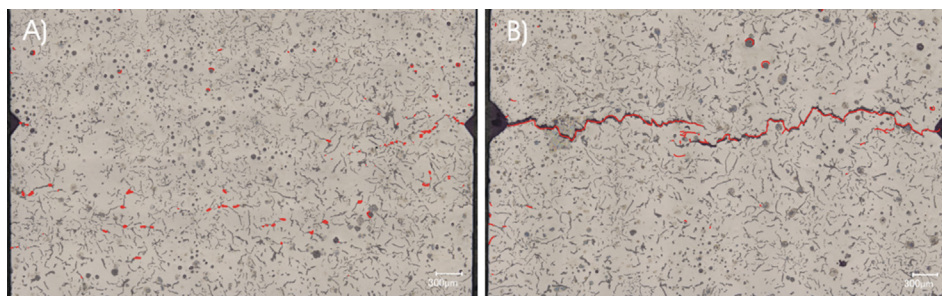


Fig. 12. Solid samples with 0.1 and 0.2 mm notches tested under total constraint mode until TMF failure.

overlapping cyclic plastic zone size [24], cf. Fig. 9.

Fig. 10 combines the latter factors and illustrates the supposed interaction of cyclic plastic zones at the delaminated graphite particles. If during the first TMF cycle, delamination occurs in an edge graphite particle, its plastic zone will be able to interact with neighboring plastic zones of delaminated bulk particles via overlapping plastic zones. Evidently, the model strongly depends on the graphite spatial distribution and orientation. It can be said that the observed crack sizes correspond to the joined sizes of graphite particles and plastic zones, affected by the

directionality of the particles.

The latter is an ideal scenario, based among others on the average distance between graphite centroids (53–66 μm). It indicates that the theoretical gap to be filled is of the order of 9–22 μm ($53 \text{ or } 66 \mu\text{m} - 2 * 44/2 \mu\text{m}$) when two graphite particles are perfectly aligned. Considering the schematic condition of Fig. 10, it is possible to obtain 10 μm and 5 μm of plastic zones from surface and bulk particles, of which the sum can fill up the gap between the particle tips. This scenario assumes that the surface particle has an equal size compared to a

bulk particle, which implicitly assumes that the particles were not cut during manufacturing. It is more probable, though, to consider that surface particles have a reduced size as they may be sectioned by the outer surface of the sample. Assuming that their length is cut in half, using Fig. 9, the plastic zone of such half graphite particle at the surface would be 5 μm . In the new scenario, the distance bridged by the dynamic plastic zones drop to 10 μm which is still within reach of the measured gap between particles.

Fig. 10 is an idealized 2D scenario where graphite particles are aligned, and where interaction with other particles is not considered. Consequently, a further step was taken in order to connect theoretical calculations with experimental data.

Since in Fig. 7 it was observed that the crack path approximately connects nearest neighbor graphite particle tips, whilst observing the external boundary condition of the applied loading direction. Hence, the distance between these nearest neighbour particle tips was considered as the crucial microstructural variable controlling the crack propagation features. Therefore, this variable was quantified on the 2D image, cf. Fig. 11. A rigorous analysis was carried out, whereby the distance between nearest neighbour graphite particle tips was mapped, cf. Fig. 11a. Due to the irregular shape of the particles, it was not always immediately clear from visual inspection which was the nearest particle tip. Therefore, for each graphite particle tip, three candidate nearest neighbours were selected and the minimum distance for each of the 3 candidates was recorded. A database of 200 data points was collected for which the distribution is presented in Fig. 11b. This distribution exhibits an average value of 20.6 μm . Considering the fact that the combined plastic zones size are in the range of 15–10 μm at the particle tip, it can be seen from the distribution of Fig. 11b that 25% of neighboring graphite particles are close enough to have the inter-particle distance to be entirely bridged by the (cyclic) plastic zone, which will favor the cracks at the tips of these neighboring particles to be merged. The latter validates the proposed crack initiation event and it is in accordance with experimental results where it was observed that few (about 9.5%) graphite particles on the surface led to cracks linking graphite particles.

Considering the previous analysis, and in order to further analyze the crack initiation phenomena a second approach to link theory and real data was performed. Smooth and notched (0.1, 0.2, 0.35, 0.5, 0.6 mm) TMF specimens (standard samples not semi in-situ) were tested until failure under total constraint [24]. A sample is considered to fail when a micro crack becomes a macro crack [33] and therefore the bulk maximum stress is reduced. It was found that some of the 0.1 mm notched specimens presented a mixed crack failure initiation; i.e. the crack initiated in or out of the notch (cf. Fig. 12A). This is in contrast with the failure mode found in 0.2 mm notched specimens, where the crack was propagated within the notched area (cf. Fig. 12B). For samples with larger notch size, all of the cracks have initiated at the notch. For the 0.1 mm notched specimens, it can be said that the stress concentration due to delaminated particles at the sample surface lead to interaction of cyclic plastic zones and therefore larger stress concentration than the machined 0.1 mm notch. In other words, the stress concentration at graphite particles could produce a 80 to 120 μm crack, which is comparable to the cracks observed at the 0.1 mm notched sample.

Based on these observations, a correction to the concept of “notch size” is proposed for smooth specimens. At this point, it has been shown that at the sample surface of smooth specimens most of the graphite particles were delaminated (irrespective of the direction with respect to the loading direction). However, it was experimentally observed that less than 10% of this population was involved in surface crack initiation (crack linking graphite particles) due to the interaction conditions previously described. Since the minimum observed crack length joining graphite particles was 80 μm , it is reasonable to assume that the smooth solid specimens tested under TMF developed cracks during the first cycle of which the length was at least 80 μm .

5. Conclusion

Although, it is known that crack initiation is an early event on CGI under OP-TMF regimes, only by performing the semi in-situ test it was possible to differentiate the stage of crack initiation by delamination and early growth. The described innovative technique was successfully executed making it possible to identify that CGI samples under total constraint experienced bulk and edge delamination followed by edge crack initiation and short edge crack propagation as a result of merging of delaminated edge graphite particles during the tensile part of the first TMF cycle.

It was calculated that the cyclic plastic zone of graphite particles in contact with the surface might be larger than the cyclic plastic zone associated with bulk particles. This leads to an increase of the probabilities of interaction between particles at the surface and therefore crack initiation at the sample surface. In this scenario crack initiation is enhanced by the presence of graphite clusters. In such areas, the distance between graphite surfaces is reduced and the plastic zones at the tip of delamination cracks are more likely to connect.

Considering the KAM maps derived from EBSD measurements, the dedicated setup allowed to observe the competition between recovery and cyclic plastic strain during the first TMF cycles. In general, after the first cycle a subtle microstructural hardening effect was observed. The described observations, measurements and conclusions are relevant in view of the importance of understanding the complex phenomena occurring during the first TMF cycles.

Authorship contribution statement

Edwin A. Lopez-Covaleda: Conceptualization, Methodology, Formal analysis, Investigation, Data curation, Writing - original draft, Writing - review & editing, Visualization. **Sepideh Ghodrati:** Methodology, Formal analysis, Writing - review & editing, Supervision. **Leo A.I. Kestens:** Methodology, Formal analysis, Resources, Writing - review & editing, Supervision, Project administration, Funding acquisition.

Declaration of Competing Interest

The authors declare that they have no known competing financial interests or personal relationships that could have appeared to influence the work reported in this paper.

Acknowledgements

The authors are indebted to Dr. A.C. Riemsag for ample valuable discussions and technical support.

Funding

This research was carried out under project number F23.5.13484a. in the framework of the Partnership Program of the Materials Innovation Institute M2i (www.m2i.nl) and the Foundation of Fundamental Research on Matter (FOM) (www.fom.nl), which is part of the Netherlands Organization for Scientific Research (www.nwo.nl).

References

- [1] Krakhmalev P, Yadroitsava I, Fredriksson G, Yadroitsev I. In situ heat treatment in selective laser melted martensitic AISI 420 stainless steels. *Mater Des* 2015;87:380–5.
- [2] Julien R, Velay V, Vidal V, Dahan Y, Forestier R, Rézai-Aria F. Tensile behaviour of high temperature forged Ti-6Al-4V during in-situ heat treatments. *Mater Lett* 2017;208:7–9.
- [3] Cai Z, et al. Fracture behavior of high-entropy alloy coating by in-situ TEM tensile testing. *J Alloy Compd* 2017;729:897–902.
- [4] Cai Z, Cui X, Jin G, Lu B, Zhang D, Zhang Z. In situ TEM tensile testing on high-

- entropy alloy coating by laser surface alloying. *J Alloy Compd* 2017;708:380–4.
- [5] Ye XX, et al. Strengthening-toughening mechanism study of powder metallurgy Ti-Si alloy by interrupted in-situ tensile tests. *J Alloy Compd* 2017;694:82–92.
- [6] Haddad M, Ivanisenko Y, Courtois-Manara E, Fecht H-J. In-situ tensile test of high strength nanocrystalline bainitic steel. *Mater Sci Eng, A* 2015;620:30–5.
- [7] Zhao PJ, Chen ZH, Dong CF. Failure analysis based on microvoids damage model for DP600 steel on in-situ tensile tests. *Eng Fract Mech* 2016;154:152–68.
- [8] Van Petegem S, et al. A miniaturized biaxial deformation rig for in situ mechanical testing. *Exp Mech* 2017; 57(4): 569–580 [2017/04/01].
- [9] Sun Z, Van Petegem S, Cervellino A, Blum W, Van Swygenhoven H. Grain size and alloying effects on dynamic recovery in nanocrystalline metals. *Acta Mater* 2016;119:104–14.
- [10] Mazars V, et al. Damage investigation and modeling of 3D woven ceramic matrix composites from X-ray tomography in-situ tensile tests. *Acta Mater* 2017;140:130–9.
- [11] GmbH DFM. Thermomechanical Fatigue Life Prediction of Cylinder Heads in Combustion Engines. *J Eng Gas Turbines Power* 2008;130(012806–1):10.
- [12] Steve Dawson S. Compacted graphite iron A material solution for modern diesel engine cylinder blocks and heads. *China Foundry* 2009; 241(06): p. 6, 2009.
- [13] Li J, Wang P, Cui X, Li K, Yi R. Gray cast iron cylinder head thermal mechanical fatigue analysis. In: FISITA 2012 world automotive congress, Berlin, vol. 189. Springer Berlin Heidelberg; 2013. pp. 243–257.
- [14] Norman V, Skoglund P, Leidermark D, Moverare J. The effect of superimposed high-cycle fatigue on thermo-mechanical fatigue in cast iron. *Int J Fatigue* 2016;88:121–31.
- [15] Norman V, Skoglund P, Leidermark D, Moverare J. Thermo-mechanical and superimposed high-cycle fatigue interactions in compacted graphite iron. *Int J Fatigue* 2015;80:381–90.
- [16] Metzger M, Nieweg B, Schweizer C, Seifert T. Lifetime prediction of cast iron materials under combined thermomechanical fatigue and high cycle fatigue loading using a mechanism based model. *Int J Fatigue* 2013;53:58–66.
- [17] Ghodrat S, Rienslag AC, Janssen M, Sietsma J, Kestens LAI. Measurement and characterization of Thermo-Mechanical Fatigue in Compacted Graphite Iron. *Int J Fatigue* 2013;48:319–29.
- [18] Collin N. Thermo-mechanical fatigue of cast iron for engine applications. Master of Science, Industrial Engineering and Management, KTH, Stockholm; 2014.
- [19] Hosseini E, Holdsworth SR. Cracking due to combined TMF and HCF loading in cast iron. *Int J Fatigue* 2017;99:279–85.
- [20] Zhang W, Liu Y. Investigation of incremental fatigue crack growth mechanisms using in situ SEM testing. *Int J Fatigue* 2012;42:14–23.
- [21] Jacobsson L, Persson C, Melin S. In-situ ESEM study of thermo-mechanical fatigue crack propagation. *Mater Sci Eng, A* 2008;496(1):200–8.
- [22] Norman V, Calmunger M. On the micro- and macroscopic elastoplastic deformation behaviour of cast iron when subjected to cyclic loading. *Int J Plast* 2018.
- [23] Hahner P, et al. Research and development into a European code of practice for strain controlled thermo mechanical fatigue testing. *Int J Fatigue* 2008; 30(2): pp. 372–381.
- [24] Lopez-Covaleda EA, Ghodrat S, Kestens LAI. Lifetime and damage characterization of compacted graphite iron during thermo-mechanical fatigue under varying constraint conditions. *Metall and Mat Trans A* 2019; [2019/11/06].
- [25] Rueden CT, et al. ImageJ2: ImageJ for the next generation of scientific image data. *BMC Bioinform* 2017; 18(1): p. 529 [2017/11/29].
- [26] Kalra A. “Thermo-Mechanical Fatigue-Lifetime Determination of Diesel Engine Exhaust Manifolds,” Master of Science, 3Mi. Delft: Delft University of Technology; 2016.
- [27] Christ HJ, Jung A, Maier HJ, Teteruk R. Thermomechanical fatigue damage mechanisms and mechanism based life prediction methods. *Sadhana* 2003;28(1):147–65.
- [28] Anderson TL. *Fracture Mechanics: Fundamentals and Applications*, 3 ed. CRC Press; 2004, p. 640.
- [29] Tada H, Paris PC, Irwin GR. Stress analysis results for common test specimen configurations. In: Tada H, Paris PC, Irwin GR, editors. *The Stress Analysis of Cracks Handbook*, third ed. New York, NY: ASME; 2000.
- [30] Lopez-Covaleda E, Ghodrat S, Kestens L, Sacre C-H, Pardoën T. Proposal of characterization procedure of metal-graphite interface strength in compacted graphite iron. *Mater* 2018; 11(7).
- [31] Uguz A, Martin JW. Plastic zone size measurement techniques for metallic materials. *Mater Charact* 1996;37(2):105–18.
- [32] Ghodrat S, Rienslag A, Kestens L. Measuring Plasticity with Orientation Contrast Microscopy in Aluminium 6061-T4. *Metals* 2017;7(4):108.
- [33] Norman V, Skoglund P, Leidermark D, Moverare J. The transition from micro- to macrocrack growth in compacted graphite iron subjected to thermo-mechanical fatigue. *Eng Fract Mech* 2017;186:268–82.